Manipulating Local Chemistry of Phosphorus for High-Performance Sodium Ion Battery Anode Applications

Danni Lan and Quan Li*

Department of Physics, The Chinese University of Hong Kong, Shatin, New Territory, Hong Kong, China

S Supporting Information

ABSTRACT: The manipulation of the chemical environment of P by forming phosphorus-titania−carbon (P−TiO$_2$−C) composite leads to a high-performance anode material with a reversible capacity of 1147 mA h g^{-1} at a current density of 100 mA g^{-1}, a high rate capacity retention of 81.5% for charging/discharging rate increasing from 100 to 1000 mA g^{-1}, and a good cycle stability (540 mA h g^{-1} at a current density of 1 A g^{-1} is maintained after 100 cycles). The excellent electrochemical properties of the composite anode originate from the changed chemical states of both TiO$_2$ and P, providing an effective strategy in designing high-performance sodium ion battery anode materials.
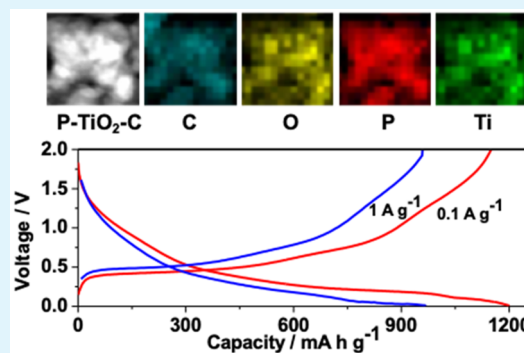
KEYWORDS: phosphorus, titanium oxide, local chemistry, anode, sodium ion batteries

Phosphorus (P) has been considered as a promising anode material for sodium ion batteries (SIBs), due to its high theoretical capacity (2596 mA h g^{-1}) and reasonably low redox potential (∼0.45 V vs Na/Na$^+$), implying achievable high energy density.[1−15] However, the intrinsic low conductivities (∼10^{-14} S cm^{-1}), the huge volume expansion (390% of its original volume), and the instability of the P species in the electrolyte result in low practical capacity, inferior cycle stability, as well as low initial Coulombic efficiency for the phase pure P-based anodes.[16−23]

Numerous attempts have been made to tackle the above outstanding issues, aiming to achieve high reversible capacity and cycle stability simultaneously. Forming phosphide is found to improve cycle stability of the anode but at the expense of significantly reduced capacities far below the respective theoretical values of these materials.[8,24−32] Recent work of P-core/phosphide-shell leads to significantly improved electrochemical properties, representing an alternative phosphide-based approach to stabilize the P during cycling while maintaining its reversible high capacity.[10] On the other hand, composite approaches using P and C appear to be promising, and demonstrations of very high capacity (∼1900 mA h g^{-1}) and long cycle life are recently shown in a P−C composite fabricated by thermal evaporation methods.[16] Nonetheless, the performance of the P−C composites are found to be dependent on their fabrication methods.[33] The large amount of carbon (usually ≥30%)[10] in the composite is also a concern. The low density (∼2.16 g cm^{-3} for carbon materials)[34], high specific area, poor air stability and low operating voltage (<0.1 V vs Na/Na$^+$)[35] of these carbonaceous materials usually result in low volumetric capacity, low Coulombic efficiency, auto-ignition (e.g., some P/C samples are flammable in air), and

possible sodium plating in the composites electrodes.[10,12,21,36−38] The higher the carbon content, the more significant these problems are. In this regard, reduced carbon content in the electrode, if not a complete elimination, is desired, and search of non-carbonaceous materials that can carry out similar functions as those of carbon is in need.

A possible candidate for such an application is TiO$_2$, which is a low cost and environmentally friendly ceramic with high density (3−5 g cm^{-3}, depends on the crystal phases)[34], high air stability, and suitable sodiation/desodiation potentials (∼0.7 V vs Na/Na$^+$). In fact, it has been studied as an anode itself, or as stable matrix to enhance the electrochemical performance of the Sb-based and Sn-based anodes in SIBs.[39−45] However, it remains unclear whether TiO$_2$ can work with P, in which case one would need synergistic mechanisms that can enhance the electronic conductivity of TiO$_2$ (intrinsically low electronic conductivity ∼10^{-12} S cm^{-1})[39] as well as provide a suitable chemical environment for phosphorus so that it can survive the cycling process and release high capacity.

In the present work, we have synthesized P−TiO$_2$−C composites by a simple, low-cost, and easily scalable high-energy ball milling (HEBM) method. We show that the introduction of TiO$_2$ leads to a composite anode with higher capacity, higher rate performance, and comparable cycle stability to that of P−C composite fabricated with the same method. Detailed studies on the chemical states of the compositional elements before and after the composite electrode formation disclose the origin of the superior
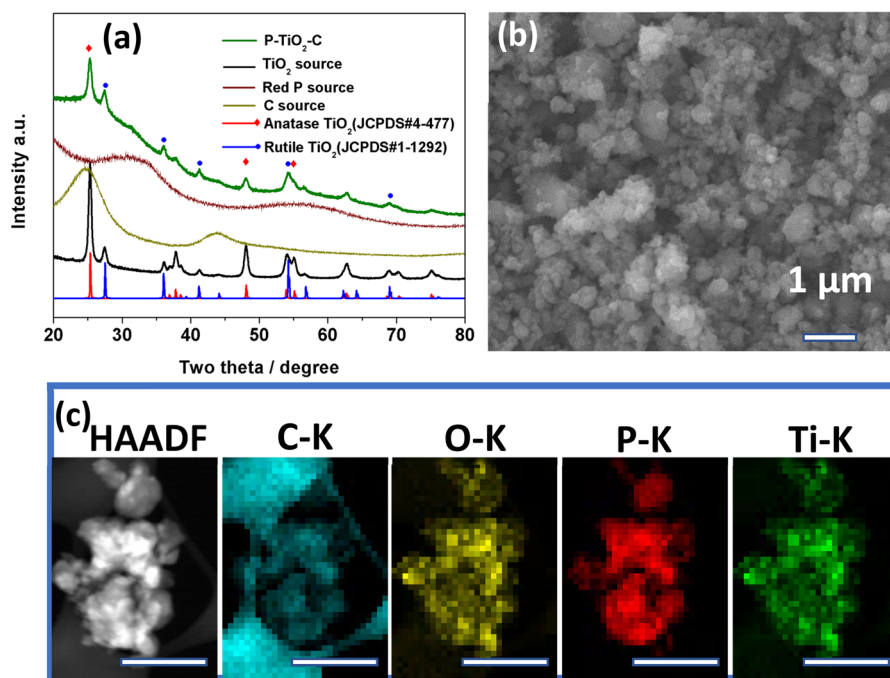
Figure 1. (a) XRD patterns of the P−TiO₂−C composite sample; the XRD results of the P, TiO₂, and C source materials are also shown for comparison. (b) SEM image showing the particle like morphology of the sample. (c) STEM high-angle annular dark field image and EDS maps of the P−TiO₂−C composites. The scale bar is 250 nm.

performance of the electrode, that is, the modified local chemistry of both TiO₂ and P in the composite sample. The present work sheds light on the general understanding of manipulating the chemical environment in the electrode material for improved electrochemical performance and provides an effective strategy for designing high-performance sodium ion battery anode.

Figure 1a shows the X-ray powder diffraction (XRD) patterns of the as-milled P−TiO₂−C composites with an optimized weight ratio of P/TiO₂/C as 6:2:2 (Figure S1). XRD taken from the starting source material of P, C, and TiO₂ are also shown for comparison. The main diffraction peaks can be indexed to those of anatase and rutile TiO₂ (JCPDS no. 1-1292 and 4-477 for rutile and anatase TiO₂, respectively). No other distinct diffraction peak is found, suggesting the poor crystallinity/amorphous nature of both red P and carbon in the composite sample. This is consistent with the TEM observation of the sample (Figure S2), i.e., one can see small crystallites of ∼15 nm embedded in an amorphous background. Compared to the source TiO₂, the increased full width at half maximum (fwhm) (Figure S3) of the corresponding diffraction peaks suggest deteriorated crystallinity of TiO₂ in the composite after ball milling. Figure 1b shows the scanning electron microscopy (SEM) image of the composites, in which featureless particles with diameters ranging from hundreds of nanometers to ∼1 μm appear to be agglomerated. Figure 1c shows the HAADF image and the corresponding energy dispersive spectrometer (EDS) maps of the composite sample. A mixture of P, C, Ti, and O can be found, while the Ti signal always overlaps with that of O, and a mismatch among P, C, and Ti/O is constantly observed below a ∼100 nm scale.

Figure 2a compares the Raman spectra of C, TiO₂, red P starting materials, and the P−TiO₂−C composite. The two bands at 1352 and 1589 cm⁻¹ observed in the C starting material (green) are known as the defect-induced (D) band
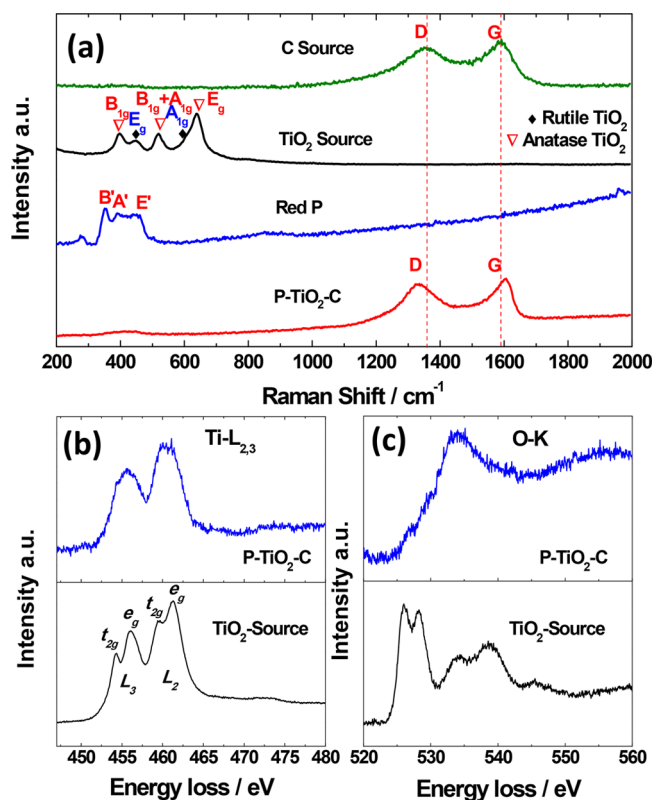
Figure 2. (a) Raman spectra comparison of the P−TiO₂−C composites and the red P, TiO₂, and C starting materials. (b) EELS Ti L₂,₃-edge fine structure comparison of the P−TiO₂−C and TiO₂ starting materials. (c) O K edge fine structures taken from the same sample as (b).

and graphitic-induced (G) band of carbon.[46] The Raman spectrum taken from TiO₂ (black) shows three bands at 397,
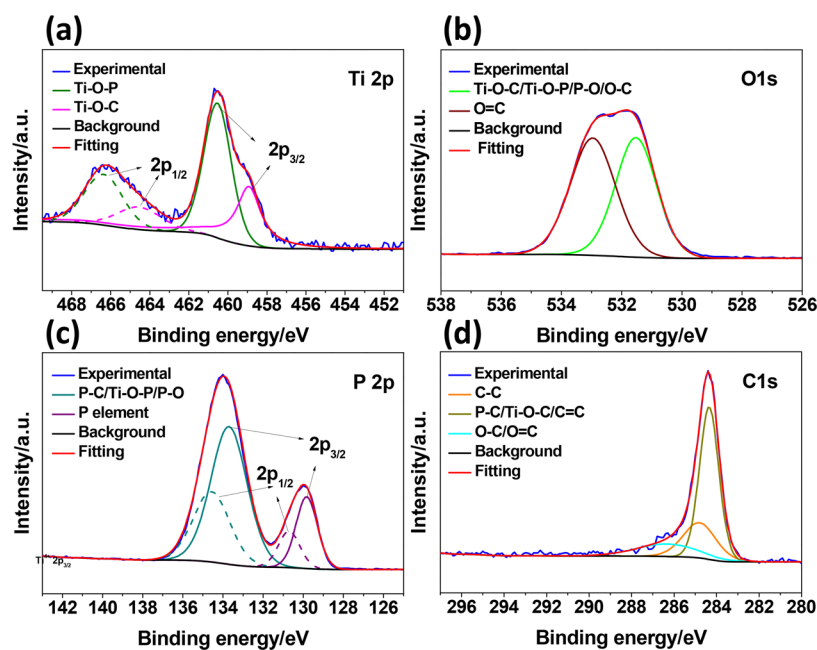
Figure 3. XPS results of (a) Ti 2p, (b) O 1s, (c) P 2p, and (d) C 1s of the P−TiO$_2$−C composites.

517, and 637 cm^{-1}, being characteristic of anatase TiO$_2$.[47] The shoulder at 610 cm^{-1} and the small peak at 448 cm^{-1} come from the rutile phase[48] of the same material. The Raman spectrum of the P source (blue) shows three bands from ∼300 to 500 cm^{-1}, which can be assigned to the B^1, A^1, and E^1 modes of red P.[49] After ball milling, the D and G bands preserve in the Raman spectrum of P−TiO$_2$−C composite (red) but shift to 1337 and 1606 cm^{-1}, respectively. A shoulder at ∼400 cm^{-1} can be found in the same spectrum, but features being characteristic of TiO or P are lost. The downshift of the D band and the upshift of the G band suggest change in the structure of the original carbon owing to new defects generation.[50] The disappearance of the spectra fingerprints in the cases of red P and TiO$_2$ indicates that the chemical environment of P and TiO$_2$ are likely modified. The crystallinity/structural deterioration of the TiO$_2$ after the composite formation is also evidenced in the EELS spectra taken from such a sample. Figure 2b compares the Ti L$_{2,3}$ edges of the TiO$_2$ source materials (black) and the P−TiO$_2$−C composites (blue). In the TiO$_2$ source material, the fine features of t$_{2g}$ and e$_g$ as resulted from the crystal field splitting are clearly observed in both L$_3$ and L$_2$ edges. This is determined by the local symmetry of the Ti−O tetrahedral/octahedral.[51] Then, the disappearance of the t$_{2g}$ and e$_g$ splitting in the composite suggests deterioration of the structural symmetry, likely due to the incorporation of C and/or P into the TiO$_2$ lattice. Consistent results are obtained at the O K edge (Figure 2c).

Figure 3 shows the X-ray photoelectron spectroscopy (XPS) of the compositional elements in the P−TiO$_2$−C sample. Figure 3a is a high-resolution scan of the Ti 2p peak, the fitting of which gives two sets of doublets (Ti 2p$_{3/2}$ and Ti 2p$_{1/2}$) with one set peaking at 458.93 and 464.63 eV and the other at 460.53 and 466.23 eV. Those two doublets can be attributed to the Ti−O−C[52,53] and Ti−O−P.[54,55] This represents a significant change of the Ti chemical states from the starting TiO$_2$ source material (Figure S4a) to the composite. The Ti 2p XPS of the TiO$_2$ source material is fitted by one set of doublets

at ∼458.52 and ∼464.22 eV, both of which can be attributed to Ti^{4+}, being consistent with that of TiO$_2$[56] in high purity. The observed blue shift in the composite sample (vs the source material TiO$_2$) can be understood as possible phosphorus and carbon diffusing into the lattice of TiO$_2$, in which case Ti is replaced by P or C species with higher electronegativity.[54,57] The O 1s XPS spectrum in Figure 3b can be fitted by peaks at 531.52 and 532.96 eV, corresponding to the binding energy of Ti−O−C/Ti−O−P/P−O/O−C and O=C,[58,59] respectively. The feature is completely altered from that of a typical TiO$_2$, which is centered at 529.63 eV (Figure S4b).[60] This is consistent with the changes observed in the XPS results of Ti. The presence of O=C suggests surface oxidation of the sample. The P 2p XPS are shown in Figure 3c, in which two sets of fitted doublets can be found. The doublet peaks at 129.83 and 130.7 eV are attributed to the elemental P, while the other peak pairs at 133.7 and 134.57 eV originate from chemically bonded P in P−C, Ti−O−P, and/or P−O (the chemical shifts of these binding states are too small to be distinguished).[21] The fact that the binding energy of P in the composite sample blue shifts (vs elemental P) suggests that metal phosphide is not likely formed in the composite.[61] As a comparison, the P in the source material stays in its elemental form (slight oxidation exists), as shown in Figure S4c. The C 1s spectrum taken from the composite sample is shown in Figure 3d. It can be fitted by three peaks, corresponding to C−C (284.8 eV), P−C/Ti−O−C/C=C (284.35 eV), and O−C/O=C (286.33 eV).[62] Compared to the XPS taken from the starting C material, the main peak in the composites shifts to low binding energies, likely due to the newly formed chemical bonds of P−C/Ti−O−C (Figure S4d). We have also carried out infrared spectroscopy (IR) to further examine the local chemistry of P−TiO$_2$−C composite (Figure S5). The spectra of P, TiO$_2$, and C source materials are also shown for comparison. Few features are observed in the IR spectra taken from either P or C, while a broad peak for TiO$_2$ appears at ∼500−800 cm^{-1}.[63,64] In the P−TiO$_2$−C composite, despite the peak at ∼500 cm^{-1} for the modified TiO$_2$, peaks at ∼1160
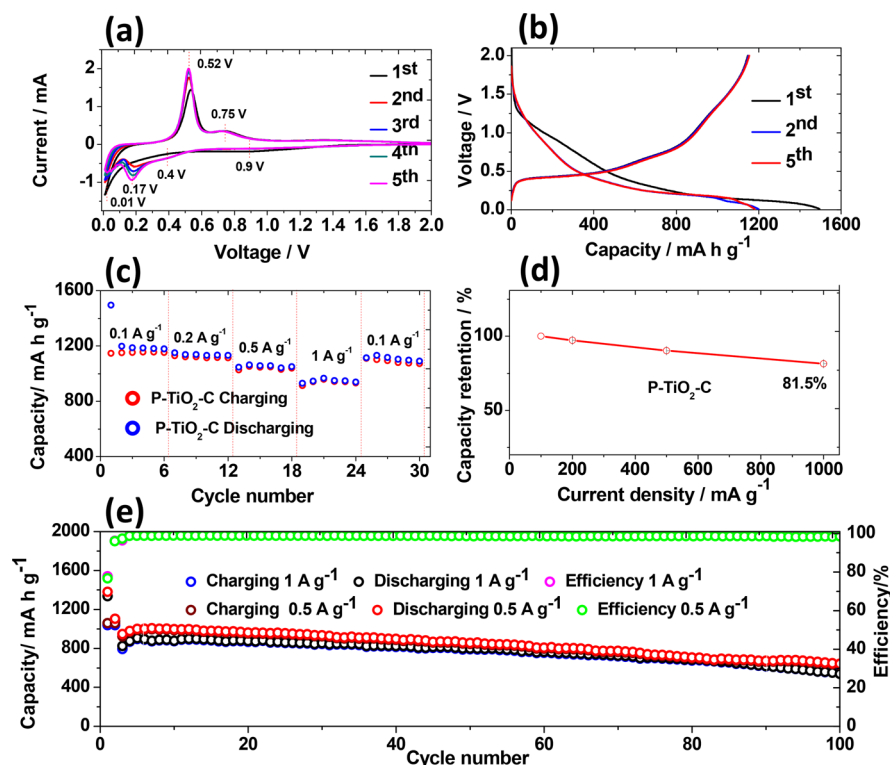
Figure 4. Electrochemical performance of the P−TiO$_2$−C composites: (a) CV plots scanned at a rate of 0.05 mV s^{-1} in the voltage range of 0.01−2 V; (b) charge/discharge curves at a constant current density of 100 mA g^{-1}; (c) rate performance measured at current densities of 100, 200, 500, and 1000 mA g^{-1}; (d) capacity retention at different current density; and (e) cycle stability measured at current densities of 0.5 and 1 A g^{-1}.

and 1005 cm^{-1} show up, which can be ascribed to the P−O/P−C[15,65] and Ti−O−P/Ti−O−C[59,66−69] bonds, respectively.

The electrochemical performance of the P−TiO$_2$−C composites anode has been evaluated by assembling them into coin cells with sodium as both the reference and counter electrode. Figure 4a shows the cyclic voltammetry (CV) profile of the P−TiO$_2$−C composites. In the initial cathodic scan, a weak and broad peak occurs at ∼0.9 V, which can be ascribed to formation of the solid electrolyte interphase (SEI). Another sharp peak appears at ∼0.01 V, corresponding to the initial sodium ion insertion and formation of Na$_x$P (1< x ≤ 3).[17] In the next four cathodic scans, despite the sodiation peak at ∼0.01 V, another two peaks centered at ∼0.4 and ∼0.17 V repeatedly show up, and the peak intensities slightly increase along with cycling. The three cathodic peaks indicate the stepwise sodiation of P during cathodic scan.[70] The potential difference between the first and later cathodic cycles as well as the increased peak intensities may be ascribed to an activation process of the electrode. In the anodic scans, repeatable peaks appear at ∼0.52 and 0.75 V, which originate from the stepwise sodium ion extraction from the charged Na$_x$P phase, being consistent with most of P-based anodes.[33,71] Although both C and TiO$_2$ are active for sodiation/desodiation, their respective capacities (theoretical values of both around 300 mA h g^{-1})[72,73] are significantly lower than that of P (theoretically ∼2600 mA h g^{-1}). Considering the amount of C and TiO$_2$ in the composite sample and their respective sodiation/desodiation potentials, their redox peaks should be buried under those of P and remain indiscernible, suggesting their minor roles in contributing to the total capacity of the anode.

Figure 4b shows the charge/discharge profiles of the P−TiO$_2$−C composites in the initial five cycles. The first

discharging capacity is measured to be 1496 mA h g^{-1}, and the first charging capacity is 1147 mA h g^{-1}, corresponding to a high initial Coulombic efficiency of 77%. The capacities are calculated based on the mass of the composite including TiO$_2$ and C. Due to the little capacity contribution from the TiO$_2$ and C, the high capacity of the P−TiO$_2$−C composites would majorly originate from the active P species inside the composites (Figure S6). These are much higher when compared to the P−C composite electrode without TiO$_2$ incorporation (Figure S1). The charging capacity is stable in the subsequent cycles, suggesting that the sodiation−desodiation process is highly reversible. The rate capacity of the P−TiO$_2$−C composites is shown in Figure 4c. The anode delivers a discharge capacity of 1154.6, 1129.2, 1052.6, and 958.9 mA h g^{-1} at the current densities of 100, 200, 500, and 1000 mA g^{-1}, respectively. The capacity is retained as 81.5% when the discharge rate increases from 100 to 1000 mA g^{-1} (Figure 4d), which is much higher than the 68.5% capacity for the P−C composite electrode without TiO$_2$ incorporation (Figure S7). To reveal the cycle stability of the P−TiO$_2$−C composites, the electrode is galvanostatically discharged and charged at 100 mA g^{-1} for the first two cycles and then charged and discharged at 0.5 and 1 A g^{-1} for the following cycles (Figure 4e). The electrode can be steadily cycled for 100 cycles with a high capacity of 632 and 540 mA h g^{-1} at the current density of 0.5 and 1 A g^{-1}, respectively. The cycling performance is comparable with most of the ball milling P/C composites electrodes.[7,8] One shall note that the P−TiO$_2$−C composites show low transfer resistance after the first cycle (from EIS measurement, Figure S8), indicating its good electronic conductivity. After 100 cycles, the transfer resistance is found to increase, likely due to the possible volume change

and the chemical instibility of the elelctrode during cycling. Consequently, the deteriorated conductivity contributes to capacity fading after 100 cycles.

The excellent performance of the P−TiO$_2$−C composite anode is ascribed to the synergistic effect originating from the specific combination of P, TiO$_2$, and C. When considering the capacity, the conductivity, the volume expansion, and the stability, P, TiO$_2$, and C are complementary to each other. P has the highest theoretical capacity of ~2600 mA h g^{-1}, but it suffers from low conductivity (~10^{-14} S cm^{-1}), huge volume expansion, and instability in electrolyte during cycling. TiO$_2$ is a stable ceramic but has low capacity and electronic conductivity (~10^{-12} S cm^{-1}). C material is stable and has good conductivity but is limited by its low capacity. When compositing those three species together into P−TiO$_2$−C with creating proper chemical environments, a synergistic effect arises from the doping of TiO$_2$ by P and/or C (leading to significantly improved conductivity[55] (~3 × 10^{-4} S cm^{-1}, Table S1)), as well as stabilization of P by the Ti−O−P and/or P−C chemical environment. The higher reversible capacity of the P−TiO$_2$−C composite sample (vs P−C composite) suggests the existence of a more active chemical state of phosphorus.

The cycle life of the P−TiO$_2$−C composite electrode is limited by the presence of elemental P in the electrode. The present ball-milling method is ineffective in transferring all elemental P to those of Ti−O−P. This is also the reason why carbon is still needed to accommodate some P by forming P−C bonds. A more effective method to completely transfer elemental P to Ti−O−P is currently being sought.

In conclusion, we show that forming P−TiO$_2$−C composites leads to changes of local chemistry in both titanium oxide and phosphorus, improving the electronic conductivity of the former and stabilizing the latter during repeated sodiation/desodiation cycles. The resulting composite anode thus delivers a high reversible capacity of 1147 mA h g^{-1} at a current density of 100 mA g^{-1} with good cyclability. Such a composite electrode also shows excellent rate performance by maintaining 81.5% of its original capacity when the discharge rate increased from 100 to 1000 mA g^{-1}.

■ EXPERIMENTAL SECTION

Synthesis of the P−TiO$_2$−C Composites. Red phosphorus in size of 100 mesh and titanium oxide (an anatase and rutile titanium oxide mixture) were purchased from Aladdin Industrial Co., Ltd., and carbon powder was obtained from Sigma-Aldrich. P−TiO$_2$−C composites were prepared by ball milling under an argon atmosphere. In order to investigate an optimized ratio for the P−TiO$_2$−C composites, the weight ratio of P/TiO$_2$/C was set to 6:4:0, 6:3:1, 6:2:2, 6:0:4, and 7:2:1 for preliminary electrochemical tests. The weight ratio of milling balls (stainless steel) to powders was 20:1. The rotation speed of the mill was set to 500 rpm for 48 h.

From preliminary electrochemical tests in SIBs, the P−TiO$_2$−C composites with a ratio of 6:2:2 show the best electrochemical performance in terms of capacity and cycle stability (Figure S1), Therefore, all the data discussed in the main text refers to P−TiO$_2$−C (6:2:2) composites unless otherwise specified.

Characterization. X-ray diffraction (XRD, SmartLab, Rigaku) with a Cu−Kα radiation source (λ= 0.1541 nm) was used to characterize the crystallinity and phases of the samples. Scanning electron microscopy (SEM, JSM-7800F, JEOL) was performed to reveal the morphological features of the samples. Transmission electron microscopy (TEM)-based techniques were carried out using a Tecnai F20 ST (FEI) microscope operating at 200 kV. Element mapping taken in the STEM model was performed by using energy-dispersive X-ray spectroscopy (EDS). Electron energy loss spectroscopy (EELS) was carried out to disclose the electronic structure of the composition sample. The chemical states of the compositional elements of the samples were analyzed by X-ray photoelectron spectroscopy (XPS) (Thermo Scientific, Escalab 250Xi). The electronic conductivity of the composites was measured by a four-point probe method. Raman analysis was performed using a Micro Raman spectrometer (RM-1000, Renishaw Co., Ltd.) with a 10 mW helium−neon laser at 514 nm. The local chemistry of the samples was examined by a Fourier transform infrared spectrometer (FTIR, Nicolet 670, Thomas Nicolet, Waltham, MA).

Assembly of a 2032 Coin-Type Half-Cell with Na as the Anode. The electrodes were prepared by spreading a slurry of 70 wt % active materials (P−TiO$_2$−C composites), 20 wt % multiwalled carbon nanotubes (MWCNTs), and 10 wt % sodium carboxymethylcellulose (CMC) binder (without any other additional additive) on a copper foil substrate to form a thin film. The mass loading of the active materials within the film was about ~0.9 mg cm^{-2}. A mixture of 1 M NaClO$_4$ in propylene carbonate/fluoroethylene carbonate (PC/FEC, 95:5 in volume) was used as the electrolyte. Cyclic voltammertry (CV) scanned at a sweep rate of 0.05 mV s^{-1} and electrochemical impedance spectroscopy (EIS) performed in the frequency between 100 kHz and 10 mHz with an amplitude of 10 mV were measured on a CHI660c electrochemical workstation (ChenHua Instrument Co., China). The galvanostatic charge/discharge test was conducted on a LAND CT2001A battery test system. To reveal the cycle stability of the P−TiO$_2$−C composites, the electrode was galvanostatically discharged and charged at 100 mA g^{-1} for the first two cycles and then at 0.5 and 1 A g^{-1} for the following cycles.

■ ASSOCIATED CONTENT

Ⓢ Supporting Information

The Supporting Information is available free of charge on the ACS Publications website at DOI: 10.1021/acsaem.8b01666.

Comparison of desodation capacity of P−TiO$_2$−C composites with different P/TiO$_2$/C weight ratios (Figure S1); high-resolution TEM image of the P−TiO$_2$−C composite sample (Figure S2); comparison of the XRD patterns of the P−TiO$_2$−C composite and the starting TiO$_2$ source material (Figure S3); comparison of the XPS result of the starting TiO$_2$ source, red P source, C source, and the P−TiO$_2$−C composite (Figure S4); comparison of the infrared spectra of the P−TiO$_2$−C composite and the starting TiO$_2$ source material (Figure S5); electrochemical performance of the TiO$_2$ and C source materials (Figure S6); comparison of the rate performance and their capacity retentions of the P−TiO$_2$−C (P/TiO$_2$/C ratio of 6/2/2) composite sample and the P/C (P/C ratio of 6/4) samples (Figure S7); EIS results of the P−TiO$_2$−C composite after initial and long cycles (Figure S8); and conductivity measurement result of the P−TiO$_2$−C composites and P−C (P/C ratio of 6/4) samples from the four-point probe method (Table S1) (PDF)

■ AUTHOR INFORMATION

Corresponding Author

*E-mail: liquan@phy.cuhk.edu.hk.

ORCID Ⓒ

Quan Li: 0000-0001-8563-1802

Notes

The authors declare no competing financial interest.

ACKNOWLEDGMENTS

REFERENCES

(1) Zhou, J.; Liu, X.; Cai, W.; Zhu, Y.; Liang, J.; Zhang, K.; Lan, Y.; Jiang, Z.; Wang, G.; Qian, Y. Wet-Chemical Synthesis of Hollow Red-Phosphorus Nanospheres with Porous Shells as Anodes for High-Performance Lithium-Ion and Sodium-Ion Batteries. *Adv. Mater.* **2017**, *29*, 1700214.

(2) Zhao, D.; Li, B.; Zhang, J.; Li, X.; Xiao, D.; Fu, C.; Zhang, L.; Li, Z.; Li, J.; Cao, D.; Niu, C. A Hierarchical Phosphorus Nanobarbed Nanowire Hybrid: Its Structure and Electrochemical Properties. *Nano Lett.* **2017**, *17*, 3376−3382.

(3) Zhang, Y.; Sun, W.; Luo, Z.-Z.; Zheng, Y.; Yu, Z.; Zhang, D.; Yang, J.; Tan, H. T.; Zhu, J.; Wang, X.; Yan, Q.; Dou, S. X. Functionalized Few-layer Black Phosphorus with Super-Wettability towards Enhanced Reaction Kinetics for Rechargeable Batteries. *Nano Energy* **2017**, *40*, 576−586.

(4) Zeng, G.; Hu, X.; Zhou, B.; Chen, J.; Cao, C.; Wen, Z. Engineering Graphene with Red Phosphorus Quantum Dots for Superior Hybrid Anodes of Sodium-Ion Batteries. *Nanoscale* **2017**, *9*, 14722−14729.

(5) Yu, Z.; Song, J.; Wang, D.; Wang, D. Advanced Anode for Sodium-Ion Battery with Promising Long Cycling Stability Achieved by Tuning Phosphorus-Carbon Nanostructures. *Nano Energy* **2017**, *40*, 550−558.

(6) Yao, S.; Cui, J.; Huang, J.; Huang, J.-Q.; Chong, W. G.; Qin, L.; Mai, Y.-W.; Kim, J.-K. Rational Assembly of Hollow Microporous Carbon Spheres as P Hosts for Long-Life Sodium-Ion Batteries. *Adv. Energy Mater.* **2018**, *8*, 1702267.

(7) Yang, F.; Gao, H.; Chen, J.; Guo, Z. Phosphorus-Based Materials as the Anode for Sodium-Ion Batteries. *Small Methods* **2017**, *1*, 1700216.

(8) Xia, Q.; Li, W.; Miao, Z.; Chou, S.; Liu, H. Phosphorus and Phosphide Nanomaterials for Sodium-Ion Batteries. *Nano Res.* **2017**, *10*, 4055.

(9) Liu, Y.; Zhang, A.; Shen, C.; Liu, Q.; Cao, X.; Ma, Y.; Chen, L.; Lau, C.; Chen, T. C.; Wei, F.; Zhou, C. Red Phosphorus Nanodots on Reduced Graphene Oxide as a Flexible and Ultra-Fast Anode for Sodium-Ion Batteries. *ACS Nano* **2017**, *11*, 5530−5537.

(10) Liu, S.; Feng, J.; Bian, X.; Liu, J.; Xu, H.; An, Y. A Controlled Red Phosphorus@Ni−P Core@Shell Nanostructure as An Ultralong Cycle-Life and Superior High-Rate Anode for Sodium-Ion Batteries. *Energy Environ. Sci.* **2017**, *10*, 1222−1233.

(11) Li, W.; Hu, S.; Luo, X.; Li, Z.; Sun, X.; Li, M.; Liu, F.; Yu, Y. Confined Amorphous Red Phosphorus in MOF-Derived N-Doped Microporous Carbon as a Superior Anode for Sodium-Ion Battery. *Adv. Mater.* **2017**, *29*, 1605820.

(12) Chang, W. C.; Tseng, K. W.; Tuan, H. Y. Solution Synthesis of Iodine-Doped Red Phosphorus Nanoparticles for Lithium-Ion Battery Anodes. *Nano Lett.* **2017**, *17*, 1240−1247.

(13) He, H.; Wang, H.; Sun, D.; Shao, M.; Huang, X.; Tang, Y. N-Doped Rutile TiO$_2$/C with Significantly Enhanced Na Storage Capacity for Na-Ion Batteries. *Electrochim. Acta* **2017**, *236*, 43−52.

(14) Liu, W.; Zhi, H.; Yu, X. Recent Progress in Phosphorus Based Anode Materials for Lithium/Sodium Ion Batteries. *Energy Storage Mater.* **2019**, *16*, 290−322.

(15) Liu, W.; Yuan, X.; Yu, X. A Core-Shell Structure of Polydopamine-Coated Phosphorus-Carbon Nanotube Composite for High-Performance Sodium-Ion Batteries. *Nanoscale* **2018**, *10*, 16675−16682.

(16) Zhang, C.; Wang, X.; Liang, Q.; Liu, X.; Weng, Q.; Liu, J.; Yang, Y.; Dai, Z.; Ding, K.; Bando, Y.; Tang, J.; Golberg, D. Amorphous Phosphorus/Nitrogen-Doped Graphene Paper for Ultra-stable Sodium-Ion Batteries. *Nano Lett.* **2016**, *16*, 2054−60.

(17) Xu, G. L.; Chen, Z.; Zhong, G. M.; Liu, Y.; Yang, Y.; Ma, T.; Ren, Y.; Zuo, X.; Wu, X. H.; Zhang, X.; Amine, K. Nanostructured Black Phosphorus/Ketjenblack-Multiwalled Carbon Nanotubes Com-posite as High Performance Anode Material for Sodium-Ion Batteries. *Nano Lett.* **2016**, *16*, 3955−3965.

(18) Sun, J.; Lee, H.-W.; Pasta, M.; Sun, Y.; Liu, W.; Li, Y.; Lee, H. R.; Liu, N.; Cui, Y. Carbothermic Reduction Synthesis of Red Phosphorus-Filled 3D Carbon Material as A High-Capacity Anode for Sodium Ion Batteries. *Energy Storage Mater.* **2016**, *4*, 130−136.

(19) Li, W.-J.; Chou, S.-L.; Wang, J.-Z.; Liu, H.-K.; Dou, S.-X. Significant Enhancement of the Cycling Performance and Rate Capability of The P/C Composite via Chemical Bonding (P−C). *J. Mater. Chem. A* **2016**, *4*, 505−511.

(20) Li, W.; Yang, Z.; Li, M.; Jiang, Y.; Wei, X.; Zhong, X.; Gu, L.; Yu, Y. Amorphous Red Phosphorus Embedded in Highly Ordered Mesoporous Carbon with Superior Lithium and Sodium Storage Capacity. *Nano Lett.* **2016**, *16*, 1546−1553.

(21) Kim, S.-O.; Manthiram, A. High-Performance Red P-Based P−TiP$_2$−C Nanocomposite Anode for Lithium-Ion and Sodium-Ion Storage. *Chem. Mater.* **2016**, *28*, 5935−5942.

(22) Gao, H.; Zhou, T.; Zheng, Y.; Liu, Y.; Chen, J.; Liu, H.; Guo, Z. Integrated Carbon/Red Phosphorus/Graphene Aerogel 3D Architecture via Advanced Vapor-Redistribution for High-Energy Sodium-Ion Batteries. *Adv. Energy Mater.* **2016**, *6*, 1601037.

(23) Ni, J.; Li, L.; Lu, J. Phosphorus: An Anode of Choice for Sodium-Ion Batteries. *ACS Energy Lett.* **2018**, *3*, 1137−1144.

(24) Wang, W.; Zhang, J.; Yu, D. Y. W.; Li, Q. Improving the Cycling Stability of Sn$_4$P$_3$ Anode for Sodium-Ion Battery. *J. Power Sources* **2017**, *364*, 420−425.

(25) Lan, D.; Wang, W.; Shi, L.; Huang, Y.; Hu, L.; Li, Q. Phase Pure Sn$_4$P$_3$ Nanotops by Solution-Liquid-Solid Growth for Anode Application in Sodium Ion Batteries. *J. Mater. Chem. A* **2017**, *5*, 5791−5796.

(26) Liu, J.; Kopold, P.; Wu, C.; van Aken, P. A.; Maier, J.; Yu, Y. Uniform Yolk−Shell Sn$_4$P$_3$@C Nanospheres as High-Capacity and Cycle-Stable Anode Materials for Sodium-Ion Batteries. *Energy Environ. Sci.* **2015**, *8*, 3531−3538.

(27) Qian, J.; Xiong, Y.; Cao, Y.; Ai, X.; Yang, H. Synergistic Na-Storage Reactions in Sn$_4$P$_3$ as a High-Capacity, Cycle-Stable Anode of Na-Ion Batteries. *Nano Lett.* **2014**, *14*, 1865−9.

(28) Kim, Y.; Kim, Y.; Choi, A.; Woo, S.; Mok, D.; Choi, N. S.; Jung, Y. S.; Ryu, J. H.; Oh, S. M.; Lee, K. T. Tin Phosphide as a Promising Anode Material for Na-Ion Batteries. *Adv. Mater.* **2014**, *26*, 4139−4144.

(29) Lu, Y.; Zhou, P.; Lei, K.; Zhao, Q.; Tao, Z.; Chen, J. Selenium Phosphide (Se$_4$P$_4$) as a New and Promising Anode Material for Sodium-Ion Batteries. *Adv. Energy Mater.* **2017**, *7*, 1601973.

(30) Lan, D.; Wang, W.; Li, Q. Cu$_4$ Snp$_{10}$ as a Promising Anode Material for Sodium Ion Batteries. *Nano Energy* **2017**, *39*, 506−512.

(31) Li, W. J.; Chou, S. L.; Wang, J. Z.; Liu, H. K.; Dou, S. X. A New, Cheap, and Productive Fep Anode Material for Sodium-Ion Batteries. *Chem. Commun.* **2015**, *51*, 3682−5.

(32) Usui, H.; Domi, Y.; Yamagami, R.; Fujiwara, K.; Nishida, H.; Sakaguchi, H. Sodiation−Desodiation Reactions of Various Binary Phosphides as Novel Anode Materials of Na-Ion Battery. *ACS Appl. Mater. Interfaces* **2018**, *1*, 306−311.

(33) Fu, Y.; Wei, Q.; Zhang, G.; Sun, S. Advanced Phosphorus-Based Materials for Lithium/Sodium-Ion Batteries: Recent Developments and Future Perspectives. *Adv. Energy Mater.* **2018**, *8*, 1703058.

(34) Hanawalt, J. D.; Rinn, H. W.; Frevel, L. K. Chemical Analysis by X-ray Diffraction. *Ind. Eng. Chem., Anal. Ed.* **1938**, *10*, 457−512.

(35) Yan, D.; Yu, C.; Zhang, X.; Li, J.; Li, J.; Lu, T.; Pan, L. Enhanced Electrochemical Performances of Anatase TiO$_2$ Nanotubes by Synergetic Doping of Ni and N for Sodium-Ion Batteries. *Electrochim. Acta* **2017**, *254*, 130−139.

(36) Kim, I. T.; Kim, S.-O.; Manthiram, A. Effect of Tic Addition on SnSb−C Composite Anodes for Sodium-Ion Batteries. *J. Power Sources* **2014**, *269*, 848−854.

(37) Kim, I. T.; Allcorn, E.; Manthiram, A. Cu$_6$Sn$_5$ − TiC−C Nanocomposite Anodes for High-Performance Sodium-Ion Batteries. *J. Power Sources* **2015**, *281*, 11−17.

(38) Zhao, J.; Zhao, L.; Chihara, K.; Okada, S.; Yamaki, J.-i.; Matsumoto, S.; Kuze, S.; Nakane, K. Electrochemical and Thermal Properties of Hard Carbon-Type Anodes for Na-Ion Batteries. *J. Power Sources* **2013**, *244*, 752−757.

(39) Zhu, Y.-E.; Yang, L.; Sheng, J.; Chen, Y.; Gu, H.; Wei, J.; Zhou, Z. Fast Sodium Storage in TiO₂@CNT@C Nanorods for High-Performance Na-Ion Capacitors. *Adv. Energy Mater.* **2017**, *7*, 1701222.

(40) Ling, L.; Bai, Y.; Li, Y.; Ni, Q.; Wang, Z.; Wu, F.; Wu, C. Quick Activation of Nanoporous Anatase TiO₂ as High-Rate and Durable Anode Materials for Sodium-Ion Batteries. *ACS Appl. Mater. Interfaces* **2017**, *9*, 39432−39440.

(41) Wang, N.; Bai, Z.; Qian, Y.; Yang, J. Double-Walled Sb@TiO₂₋ₓ Nanotubes as a Superior High-Rate and Ultralong-Lifespan Anode Material for Na-Ion and Li-Ion Batteries. *Adv. Mater.* **2016**, *28*, 4126−33.

(42) Mao, M.; Yan, F.; Cui, C.; Ma, J.; Zhang, M.; Wang, T.; Wang, C. Pipe-Wire TiO₂-Sn@Carbon Nanofibers Paper Anodes for Lithium and Sodium Ion Batteries. *Nano Lett.* **2017**, *17*, 3830−3836.

(43) Wang, N.; Bai, Z.; Qian, Y.; Yang, J. One-Dimensional Yolk-Shell Sb@Ti-O-P Nanostructures as a High-Capacity and High-Rate Anode Material for Sodium Ion Batteries. *ACS Appl. Mater. Interfaces* **2017**, *9*, 447−454.

(44) Ni, J.; Fu, S.; Yuan, Y.; Ma, L.; Jiang, Y.; Li, L.; Lu, J. Boosting Sodium Storage in TiO₂ Nanotube Arrays through Surface Phosphorylation. *Adv. Mater.* **2018**, *30*, 1704337.

(45) Ni, J.; Fu, S.; Wu, C.; Maier, J.; Yu, Y.; Li, L. Self-Supported Nanotube Arrays of Sulfur-Doped TiO₂ Enabling Ultrastable and Robust Sodium Storage. *Adv. Mater.* **2016**, *28*, 2259−65.

(46) Kaufman, J. H.; Metin, S.; Saperstein, D. D. Symmetry Breaking in Nitrogen-Doped Amorphous Carbon: Infrared Observation of the Raman-Active G and G bands. *Phys. Rev. B: Condens. Matter Mater. Phys.* **1989**, *39*, 13053−13060.

(47) Ohsaka, T.; Izumi, F.; Fujiki, Y. Raman Spectrum of Anatase TiO₂. *J. Raman Spectrosc.* **1978**, *7*, 321−324.

(48) Porto, S. P. S.; Fleury, P. A.; Damen, T. C. Raman Spectra of TiO₂, MgF₂, ZnF₂, FeF₂, and MnF₂. *Phys. Rev.* **1967**, *154*, 522−526.

(49) Liu, Y.; Zhang, N.; Liu, X.; Chen, C.; Fan, L.-Z.; Jiao, L. Red Phosphorus Nanoparticles Embedded in Porous N-Doped Carbon Nanofibers as High-Performance Anode for Sodium-Ion Batteries. *Energy Storage Mater.* **2017**, *9*, 170−178.

(50) Yang, Q. H.; Hou, P. X.; Unno, M.; Yamauchi, S.; Saito, R.; Kyotani, T. Dual Raman Features of Double Coaxial Carbon Nanotubes with N-Doped and B-Doped Multiwalls. *Nano Lett.* **2005**, *5*, 2465−2469.

(51) Samet, L.; Ben Nasseur, J.; Chtourou, R.; March, K.; Stephan, O. Heat Treatment Effect on the Physical Properties of Cobalt Doped TiO₂ Sol−Gel Materials. *Mater. Charact.* **2013**, *85*, 1−12.

(52) Zegeye, T. A.; Kuo, C.-F. J.; Wotango, A. S.; Pan, C.-J.; Chen, H.-M.; Haregewoin, A. M.; Cheng, J.-H.; Su, W.-N.; Hwang, B.-J. Hybrid Nanostructured Microporous Carbon-Mesoporous Carbon Doped Titanium Dioxide/Sulfur Composite Positive Electrode Materials for Rechargeable Lithium-Sulfur Batteries. *J. Power Sources* **2016**, *324*, 239−252.

(53) Yang, C.; Zhang, X.; Qin, J.; Shen, X.; Yu, R.; Ma, M.; Liu, R. Porous Carbon-Doped TiO₂ on TiC Nanostructures for Enhanced Photocatalytic Hydrogen Production under Visible Light. *J. Catal.* **2017**, *347*, 36−44.

(54) Wu, T.; Fan, J.; Li, Q.; Shi, P.; Xu, Q.; Min, Y. Palladium Nanoparticles Anchored on Anatase Titanium Dioxide-Black Phosphorus Hybrids with Heterointerfaces: Highly Electroactive and Durable Catalysts for Ethanol Electrooxidation. *Adv. Energy Mater.* **2018**, *8*, 1701799.

(55) Ansari, S. A.; Cho, M. H. Highly Visible Light Responsive, Narrow Band Gap TiO₂ Nanoparticles Modified by Elemental Red Phosphorus for Photocatalysis and Photoelectrochemical Applications. *Sci. Rep.* **2016**, *6*, 25405.

(56) Xing, J. H.; Xia, Z. B.; Hu, J. F.; Zhang, Y. H.; Zhong, L. Growth and Crystallization of Titanium Oxide Films at Different Anodization Modes. *J. Electrochem. Soc.* **2013**, *160*, C239−C246.

(57) Madhusudanan, S. P.; Gangaja, B.; Shyla, A. G.; Nair, A. S.; Nair, S. V.; Santhanagopalan, D. Sustainable Chemical Synthesis for Phosphorus-Doping of TiO₂ Nanoparticles by Upcycling Human Urine and Impact of Doping on Energy Applications. *ACS Sustainable Chem. Eng.* **2017**, *5*, 2393−2399.

(58) He, H.; Zhang, Q.; Wang, H.; Zhang, H.; Li, J.; Peng, Z.; Tang, Y.; Shao, M. Defect-Rich TiO₂₋Δ Nanocrystals Confined in a Mooncake-Shaped Porous Carbon Matrix as an Advanced Na Ion Battery Anode. *J. Power Sources* **2017**, *354*, 179−188.

(59) Xia, Y.; Jiang, Y.; Li, F.; Xia, M.; Xue, B.; Li, Y. Effect of Calcined Atmosphere on the Photocatalytic Activity of P-doped TiO₂. *Appl. Surf. Sci.* **2014**, *289*, 306−315.

(60) Shoaib, A.; Huang, Y.; Liu, J.; Liu, J.; Xu, M.; Wang, Z.; Chen, R.; Zhang, J.; Wu, F. Ultrathin Single-Crystalline TiO₂ Nanosheets Anchored on Graphene to Be Hybrid Network for High-Rate and Long Cycle-Life Sodium Battery Electrode Application. *J. Power Sources* **2017**, *342*, 405−413.

(61) Myers, C. E.; Franzen, H. F.; Anderegg, J. W. X-Ray Photoelectron Spectra and Bonding in Transition-Metal Phosphides. *Inorg. Chem.* **1985**, *24*, 1822−1824.

(62) Cai, Y.; Wang, H. E.; Zhao, X.; Huang, F.; Wang, C.; Deng, Z.; Li, Y.; Cao, G.; Su, B. L. Walnut-like Porous Core/Shell TiO₂ with Hybridized Phases Enabling Fast and Stable Lithium Storage. *ACS Appl. Mater. Interfaces* **2017**, *9*, 10652−10663.

(63) Zhang, L.; Jiang, Y.; Li, X.; Wang, S.; Xiao, Y. Preparation of Titanium Dioxide Nanoparticles Modified with Methacrylate and Their Electrophoretic Properties. *J. Mater. Sci.: Mater. Electron.* **2015**, *26*, 5263−5269.

(64) Yen, Y.-C.; Lin, C.-C.; Chen, P.-Y.; Ko, W.-Y.; Tien, T.-R.; Lin, K.-J. Green Synthesis of Carbon Quantum Dots Embedded onto Titanium Dioxide Nanowires for Enhancing Photocurrent. *R. Soc. Open Sci.* **2017**, *4*, 161051.

(65) Zhang, F.; Dai, J.; Wang, A.; Wu, W. Investigation of the Synergistic Extraction Behavior Between Cerium (III) and Two Acidic Organophosphorus Extractants Using FT-IR, NMR and Mass Spectrometry. *Inorg. Chim. Acta* **2017**, *466*, 333−342.

(66) Liu, W.; Yuan, X.; Yu, X. A Core-Shell Structure of Polydopamine-Coated Phosphorus-Carbon Nanotube Composite for High-Performance Sodium-Ion Batteries. *Nanoscale* **2018**, *10*, 16675−16682.

(67) Lv, Y.; Yu, L.; Huang, H.; Liu, H.; Feng, Y. Preparation, Characterization of P-Doped TiO₂ Nanoparticles and Their Excellent Photocatalystic Properties under the Solar Light Irradiation. *J. Alloys Compd.* **2009**, *488*, 314−319.

(68) Li, F.; Jiang, Y.; Xia, M.; Sun, M.; Xue, B.; Liu, D.; Zhang, X. Effect of The P/Ti Ratio on the Visible-Light Photocatalytic Activity of P-Doped TiO₂. *J. Phys. Chem. C* **2009**, *113*, 18134−18141.

(69) Xia, Y.; Jiang, Y.; Li, F.; Xia, M.; Xue, B.; Li, Y. Effect of Calcined Atmosphere on The Photocatalytic Activity of P-Doped TiO₂. *Appl. Surf. Sci.* **2014**, *289*, 306−315.

(70) Guo, W.; Lin, Z.; Wang, X.; Song, G. Sonochemical Synthesis of Nanocrystalline TiO₂ By Hydrolysis of Titanium Alkoxides. *Microelectron. Eng.* **2003**, *66*, 95−101.

(71) Yu, J.; Ma, T.; Liu, S. Enhanced Photocatalytic Activity of Mesoporous TiO₂ Aggregates by Embedding Carbon Nanotubes as Electron-Transfer Channel. *Phys. Chem. Chem. Phys.* **2011**, *13*, 3491−501.

(72) Li, Y.; Chen, C.; Wang, M.; Li, W.; Wang, Y.; Jiao, L.; Yuan, H. Excellent Sodium Storage Performance of Carbon-Coated TiO₂: Assisted with Electrostatic Interaction of Surfactants. *J. Power Sources* **2017**, *361*, 326−333.

(73) Wu, C.-M.; Pan, P.-I.; Cheng, Y.-W.; Liu, C.-P.; Chang, C.-C.; Avdeev, M.; Lin, S.-k. The Mechanism of the Sodiation and Desodiation in Super P Carbon Electrode for Sodium-Ion Battery. *J. Power Sources* **2017**, *340*, 14−21.